



# Dynamic whole-body PET imaging: principles, potentials and applications

Arman Rahmim<sup>1,2</sup> · Martin A. Lodge<sup>1</sup> · Nicolas A. Karakatsanis<sup>3</sup> · Vladimir Y. Panin<sup>4</sup> · Yun Zhou<sup>1</sup> · Alan McMillan<sup>5</sup> · Steve Cho<sup>5</sup> · Habib Zaidi<sup>6</sup> · Michael E. Casey<sup>4</sup> · Richard L. Wahl<sup>7</sup>

Received: 26 April 2018 / Accepted: 28 August 2018 / Published online: 29 September 2018  
© Springer-Verlag GmbH Germany, part of Springer Nature 2018

## Abstract

**Purpose** In this article, we discuss dynamic whole-body (DWB) positron emission tomography (PET) as an imaging tool with significant clinical potential, in relation to conventional standard uptake value (SUV) imaging.

**Background** DWB PET involves dynamic data acquisition over an extended axial range, capturing tracer kinetic information that is not available with conventional static acquisition protocols. The method can be performed within reasonable clinical imaging times, and enables generation of multiple types of PET images with complementary information in a single imaging session. Importantly, DWB PET can be used to produce multi-parametric images of (i) Patlak slope (influx rate) and (ii) intercept (referred to sometimes as “distribution volume”), while also providing (iii) a conventional ‘SUV-equivalent’ image for certain protocols.

**Results** We provide an overview of ongoing efforts (primarily focused on FDG PET) and discuss potential clinically relevant applications.

**Conclusion** Overall, the framework of DWB imaging [applicable to both PET/CT(computed tomography) and PET/MRI (magnetic resonance imaging)] generates quantitative measures that may add significant value to conventional SUV image-derived measures, with limited pitfalls as we also discuss in this work.

**Keywords** PET · Dynamic · Whole-body · Parametric imaging · Kinetic modeling · Systemic disease

## Introduction

Positron emission tomography (PET) has established wide clinical acceptance, particularly for its role in oncology. In conjunction with the glucose analog 2-deoxy-2-[<sup>18</sup>F]fluoro-D-glucose (FDG), PET has become a key tool for the management of patients with a variety of malignancies as well as infections and inflammation [1]. In clinical practice, nuclear medicine physicians review the images and distinguish tumors from areas of normal physiological uptake, inflammation, or artifacts based on experience and knowledge of normal variants [2, 3]. The task is aided with the availability of anatomical information [4, 5], nowadays provided with widely available PET/CT scanners [6], and with the more recent advent of PET/MR scanners [7, 8]. Image analysis is often qualitative, with physicians providing their impressions, sometimes supported by semi-quantitative analysis particularly using the standardized uptake value (SUV). In the hands of experienced observers, this form of image assessment can be highly effective but it is also time-consuming and somewhat subjective, with potentially variable interpretations among different observers,

---

✉ Arman Rahmim  
arahmim1@jhmi.edu

<sup>1</sup> Department of Radiology and Radiological Science, Johns Hopkins University, JHOC Building Room 3245, 601 N. Caroline St, Baltimore, MD 21287, USA

<sup>2</sup> Departments of Radiology and Physics & Astronomy, University of British Columbia, Vancouver, BC V5Z 1M9, Canada

<sup>3</sup> Department of Radiology, Weill Cornell Medical College, New York, NY, USA

<sup>4</sup> Siemens Healthineers, Knoxville, TN 37932, USA

<sup>5</sup> Department of Radiology, University of Wisconsin, Madison, WI 53705, USA

<sup>6</sup> Division of Nuclear Medicine and Molecular Imaging, Geneva University Hospital, CH-1211 Geneva, Switzerland

<sup>7</sup> Mallinckrodt Institute of Radiology, Washington University School of Medicine, St. Louis, MO 63110, USA

particularly for small lesions. Overall, this methodology has documented limitations in visualizing and quantifying PET tracer uptake for a range of clinical tasks, including assessment of treatment response and distinguishing between malignant vs benign (e.g., inflammatory) uptake, especially for radiotracers which are not tumor specific, such as fluorodeoxyglucose (FDG) [2, 9–16]. Challenges can be particularly great in the post-therapy clinical setting, where potentially substantial background activities in tissues make it difficult to determine if viable tumor is present [17]. Quantitation can be a specific challenge as well, due to the time dependence of FDG uptake, with many malignant tumors having rising FDG uptake over time, with declines in normal tissue radiotracer uptake [18].

Current clinical PET protocols mirror the pattern established for traditional nuclear medicine, in that they are optimized for qualitative as opposed to quantitative assessment. The radiopharmaceutical is administered to the patient, who then typically waits for a period of time prior to image acquisition. This uptake period is to allow for the radiopharmaceutical to accumulate in the organs of interest, and in some cases for the tracer to wash out from surrounding organs [1]. However, radiopharmaceutical distribution is a dynamic process that varies substantially between tumors and normal organs and among patients [1–3]. The radiotracer uptake periods used in clinical protocols are somewhat arbitrary, based partly on convenience, and are not expected to be optimal for all clinical cases. Further delaying the start of imaging may allow for greater contrast between the organs of interest and surrounding structures [19]. However, these extended protocols suffer from additional decay of the radionuclide (leading to noisy images), and pose restrictions in routine practice (impacting workflow).

Alternative protocols involving dynamic acquisition of temporal images allow for more complete measurement of tracer kinetics. In fact, dynamic imaging has been in use for a long time in nuclear medicine [planar, single photon emission computed tomography (SPECT), and PET]. There are numerous examples in planar imaging (see [20] for some historical perspective), and multiple dynamic procedures continue to be employed. As an example, bone scintigraphy may be performed dynamically (i.e., multiple acquired frames) immediately after injection to capture perfusion information [21]. Dynamic SPECT also has a long history, going back as far as 1963 (see review in [22]), having primarily involved rotating gamma detectors, but more recently, has become significantly more feasible and popular via dedicated cardiac cameras [23]. There is significant application of dynamic cardiac PET imaging in the clinic [24]. In the case of oncologic PET imaging, quantification of tracer uptake based on compartmental modeling approaches as applied to PET images can improve both tumor characterization and treatment response monitoring [9–11, 14, 17, 25–40]. However, despite significant

potential, dynamic PET protocols, especially for oncologic FDG PET, have not translated to the clinic, partly because of their increased complexity, particularly those involving concurrent invasive blood sampling. A more significant reason is that dynamic PET acquisition is generally confined to a single bed-position limiting coverage to the axial extent of the scanner, typically 15–25 cm. However, given the importance of whole-body (WB) PET for the assessment of disseminated disease [41–45], this limited field of view is a major limitation that has prevented routine adoption of dynamic data acquisition.

In this paper, we argue that a new framework of clinical dynamic whole-body (DWB) PET imaging is both feasible and has significant potential. The promising capabilities of clinical DWB imaging are enabled by ongoing technical developments: whereas early PET systems required extended scan durations to acquire adequate count statistics, newer PET systems achieve equivalent quality at considerably shorter durations through scintillators and electronics optimized for high sensitivity 3D acquisition as well as time-of-flight detector systems [27, 46–52]. Combined with iterative image reconstruction [53], it is now possible to acquire multi-pass eyes-to-thighs imaging, achieving adequate statistical quality in less than 5 min for a single pass in FDG WB PET.

Using this multi-pass imaging strategy, it is possible to acquire and utilize valuable information from DWB images, providing an additional dimension of kinetic information that is not available with current clinical protocols. The generation of distinct kinetic data (time–activity curves, TACs) at the individual voxel-level in dynamic images enables generation of parametric images via kinetic modeling, that may hold significant value. Furthermore, as elaborated in the methodology section, a conventional ‘SUV-equivalent’ image can also be generated for certain protocols, enabling generation of multiple kinds of images from a single imaging protocol.

Overall, additional temporal data provided by DWB acquisition may significantly enhance the existing PET technique for tumor characterization. This holds significant potential to enhance diagnostic, prognostic, and treatment response monitoring capabilities of PET and to introduce an additional imaging framework in routine clinical practice. A key emphasis is that dynamic imaging and WB (or multi-bed) imaging are not mutually exclusive, and can be combined within a single PET imaging session at reasonable scan times.

## Methodology

### Addressing challenges

DWB data acquisition itself is not unprecedented in nuclear medicine. It has been employed for dosimetric assessment of radiopharmaceuticals, by performing multi-bed multi-pass

imaging, though commonly this has been performed over separate imaging sessions. The approach has also been used in multi-pass WB bone imaging (planar) [54]. In the case of routine PET imaging, however, dynamic and WB imaging have been commonly treated as distinct entities. The limited axial field-of-view of current generation PET scanners means that WB coverage requires bed translation, making it incompatible with conventional dynamic scans that acquire data continuously over a single bed position. DWB involves multi-bed, non-continuous (sparse) data acquisition over time for any given bed position, which can result in generation of noisy images. A solution to this has been to consider only 2–3 bed positions for dynamic imaging in a single imaging session, and to perform quantitative analysis at the region-of-interest (ROI) level [31, 55–57]. Nonetheless, as alluded to in the introduction, with current-generation PET scanners, it is now possible to produce high quality images with frame durations as short as 30 s/bed. This has enabled completion of multi-pass multi-bed PET acquisitions in reasonable scan times (e.g., six passes with six or seven beds/pass in 30 min or less). Figure 1 illustrates a typical DWB PET data acquisition scheme.

DWB images generated from such a protocol can be combined to generate so-called parametric images of subjects at the individual voxel level across the body [58–60]. An excellent tool to this end is Patlak kinetic modeling analysis [61, 62], also known as Patlak plot, Gjedde–Patlak plot or Patlak–Rutland plot, due to parallel formulations by different authors [63–65]. Patlak analysis has been previously applied to single-bed dynamic imaging for a number of radiotracers used in

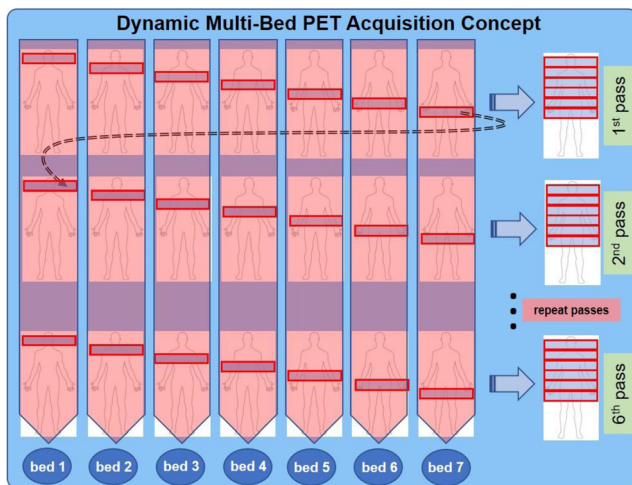


**Fig. 1** An example of a multi-pass multi-bed PET data acquisition protocol. WB imaging can refer to coverage of entire body, or more routinely, head-to-thigh imaging; e.g., using seven bed positions as shown in the figure. The example shown is that of step-and-shoot uni-directional (cranio-caudal) imaging [58, 59], but it is also possible to perform DWB imaging in continuous-bed-motion as discussed later. It is also possible to perform bi-directional imaging, while noting that this would result in differing spaces between temporal samples for different body positions

clinical imaging; e.g.,  $^{18}\text{F}$ -FDG [17, 28–38, 40],  $^{18}\text{F}$ -FLT [66–70],  $^{18}\text{F}$ -NaF [71, 72],  $^{68}\text{Ga}$ -DOTATATE and  $^{68}\text{Ga}$ -DOTOTOC [73–75]. It is, in fact, particularly suitable for analysis of DWB images, given the fact that each body position is scanned non-continuously in DWB PET. Unlike classical compartmental model fitting methods [76, 77], Patlak analysis has the advantages that: (i) it does not require PET scans to sample the early tracer kinetics, and (ii) it involves a linear fit, and thus the slope and intercept can theoretically be determined from as few as two PET measurements of a given bed position [78]. The latter is true as long as PET images are obtained after relative equilibrium is reached between the vascular and reversible tissue compartments (e.g., after 5–10 min for FDG). Indeed, more general kinetic modeling approaches remain to be carefully validated with DWB, and our subsequent discussion focuses mainly on Patlak modeling and imaging.

Let us consider a sequence of dynamic PET datasets acquired over time, and let us focus on activity concentration  $C(t)$  in the reconstructed images for a given ROI or voxel of interest. The Patlak formulation is:

$$\frac{C(t)}{C_p(t)} = K_i \frac{\int_0^t C_p(\tau) d\tau}{C_p(t)} + V \quad (1)$$

where  $C_p(t)$  is the plasma concentration over time or so-called plasma input function (PIF) (see ‘PIF estimation’ subsection below),  $K_i$  (Patlak slope) is the tracer influx or uptake rate constant, and  $V$  (Patlak intercept) is sometimes referred to as the distribution volume. It is seen that this is a linear equation, where the Patlak slope and intercept need to be estimated for every ROI or voxel of interest. If applied to every voxel, this will then produce parametric images of Patlak slope as well as intercept. We also point out that the Patlak intercept  $V$  equals  $V_0 + V_p$  where (i)  $V_0$  is the so-called initial or exchangeable volume of distribution for the reversible tissue compartment(s) (unmetabolized or unphosphorylated FDG in tissue) [64, 77, 79], and (ii)  $V_p$  is the fractional blood volume present in the ROI or voxel of interest. To see the Patlak formulation more explicitly, let us now consider the commonly used two-tissue compartmental model for FDG as shown in Fig. 2. In this case, it turns out that [76, 77]:

$$K_i = \frac{K_1 k_3}{k_2 + k_3} \quad (2)$$

$$V = V_0 + V_p = \frac{K_1 k_2}{(k_2 + k_3)^2} + V_p \quad (3)$$

$K_i$  in this case represents the overall rate of tracer uptake into the final compartment, and has been a parameter of significant interest in the literature. In any case, we emphasize

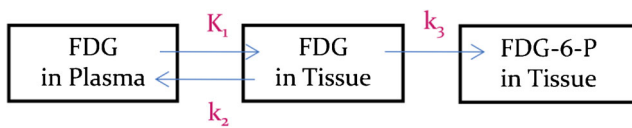


**Fig. 2** Commonly invoked two-tissue compartmental model for FDG. As a glucose analog, FDG is taken up by high-glucose-using cells, and subsequent to phosphorylation of FDG, producing  $^{18}\text{F}$ -FDG-6-phosphate, the radiotracer is nearly trapped and prevented from being released again from the cell ( $k_4$ , in the opposite direction to  $k_3$ , is commonly assumed to be negligible, thus not shown, and the last compartment is treated as effectively irreversible). A similar compartmental model is used for some other radiotracers

that the two-tissue compartment model [thus Eq. (2) and (3)] need not be assumed. In fact, Patlak formulation (1) does *not* presuppose a fixed number of compartments and is applicable to models with different numbers of compartments when tissue compartment with no or very small reversibility is assumed. In those cases,  $K_i$  and  $V$  would have different formulas than Eq. (2) and (3), but their effective meaning would be similar.

As mentioned above, one may fit and estimate Patlak slope  $K_i$  and intercept  $V$  measures at each voxel across the body, resulting in WB parametric images in DWB data acquisition. Furthermore, if PET acquisition spans times at which typical SUV images are obtained (e.g., 50–80 min post-injection), conventional SUV images may also be generated, either by summing up the corresponding passes of the DWB PET scan [80–82] or through a subsequent static WB PET scan at that time. Figure 3 shows an example where parametric Patlak slope and intercept images are generated, in addition to image-summed SUV-equivalent images. Thus, three distinct PET images can be obtained from a single PET exam. It is readily seen that the slope image has significantly reduced background uptake (e.g., in liver), while high background PET signals are observed in the intercept and SUV images.

It is instructive to link  $K_i$  to conventional SUV for FDG-avid tissues. Let us make two assumptions, namely that: (i)  $V$  is negligible (i.e., specific uptake far outweighs presence of background uptake), and (ii) the integral of the PIF ( $\int_0^t C_p(\tau) d\tau$ ) is proportional to the injected dose  $D$  divided by the weight  $W$  of the patient. In this case, re-arranging Eq. (1), one arrives at [11]:

$$K_i \approx \frac{C(t)}{\int_0^t C_p(\tau) d\tau} \propto \frac{C(t)}{D/W} = \text{SUV} \quad (4)$$

However, both assumptions can fail, resulting in considerable errors in estimated uptake rates [9–12, 29, 40]. The first assumption can be especially invalid in earlier scan times, in less FDG-avid tumors, or in the presence of substantial blood volume. Moreover, a high physiologic (non-specific) uptake may also interfere with disease-specific uptake in the same

tissue, for example when patients fail to adhere to special diet prior to the PET exam [84]. The second assumption can also be invalid. An example is when tracer infiltration/extravasation occurs at injection site, affecting the relationship between the PIF integral (radiotracer quantity available for uptake) and the total administered dosage (accounted by SUV). PIF may also be modified after a treatment regimen (e.g., chemo or hormone therapy) or by an altered cardiac output (slow cardiac output may slow clearance of radiotracer). In such cases, SUV calculation would not take PIF modification into account [11]. The resulting observed changes in SUV may then be due to the modified PIF (radiotracer quantity available for uptake) rather than an actual change in tumor uptake. By contrast, quantitative Patlak imaging is better positioned to account for these changes.

One may also take note of the method of dual-time-point FDG PET imaging, wherein the percent change in SUV uptake from an early scan (60 min) to a late scan (90–180 min) is quantified [85–87]. This method tackles the first assumption above by providing a framework to quantify rate of specific tumor uptake, instead of lumping it in with background uptake. Nonetheless, the above-mentioned problem with the second assumption remains in dual-time-point imaging. Furthermore, dual-time-point imaging requires significantly increased patient involvement, including waiting in-between scans and the added scan itself.

Next, we elaborate on some of the challenges in generating parametric Patlak images.

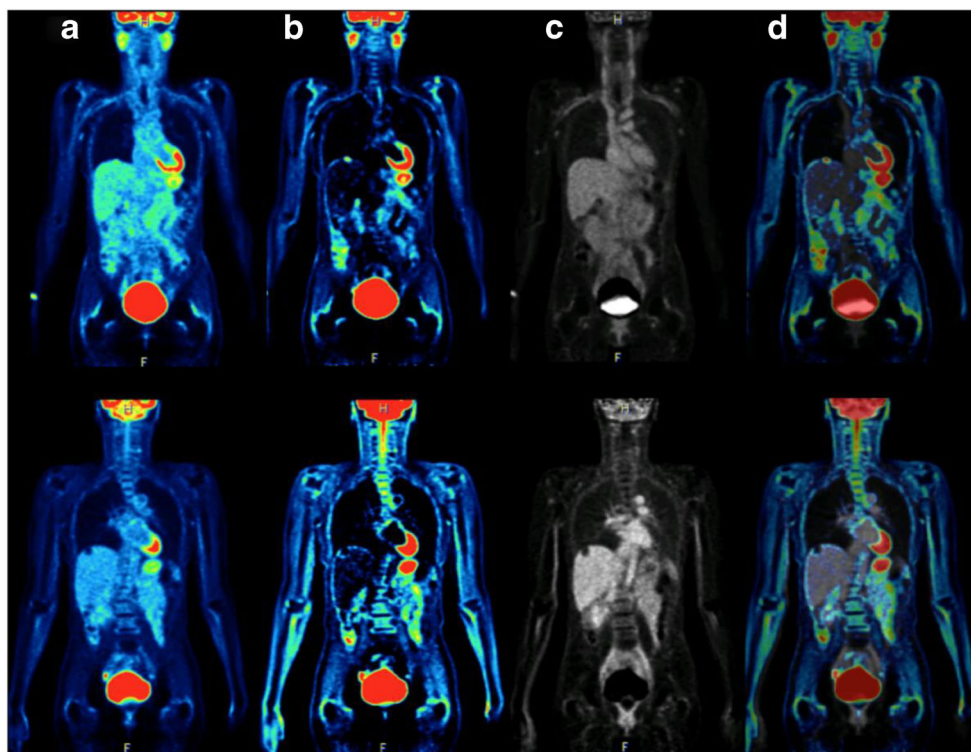
## PIF estimation

One reason dynamic PET imaging is not routinely employed in clinical imaging is the notion that estimating the PIF is difficult. This often suggests the need for invasive arterial or venous blood sampling. Nonetheless, image-derived PIF estimation is a viable alternative [88–90], and in fact is routinely employed in quantitative myocardial blood flow imaging [91, 92]. Sampling of voxels within the left ventricle or atrium are common options [93]. The challenge in past applications has been that, for single-bed dynamic imaging of organs where the heart is not in the field-of-view, one may need to utilize other blood pools such as the carotid arteries, ascending aorta, thoracic (descending) aorta, or abdominal aorta [94, 95]. These approaches may involve more difficult ROI placement, though evidence has been provided that use of ascending or abdominal aorta may be as effective as, or even more effective than using the left ventricle for input function estimation [95]. The partial volume effect also contributes differently depending on blood pool. This is an issue for smaller blood pools, but is also an issue for the left ventricle or atrium in FDG PET due to high contrast between myocardium and cavities.

The interesting advantage of DWB imaging is that a given blood pool of choice is naturally scanned at multiple time



**Fig. 3** Comparison between **a** SUV images (70–90 min post FDG injection) and parametric images (0–90 min) of **b**  $K_i$  and **c**  $V$  generated from a human DWB FDG PET scan using Patlak plot with image-derived input function and a linear regression with spatial constraint algorithm [81]. **d** Fusion of  $K_i$  on  $V$  images. *Top and bottom rows show anterior and more posterior coronal images of the patient. For routine clinically-realistic imaging, shortened DWB protocols are possible (< 30 min duration) [80, 83], which we also discuss in the text*



points within the DWB data acquisition protocol. Subsequently, these measurements can be combined with either (i) early dedicated scanning of the blood pool in the protocol (e.g., making use of the left ventricle, atrium, or aorta [59, 83]), or (ii) use of population-based PIFs [96–100] to obtain an estimate for the overall PIF. The resulting PIF is then inserted into eq. (1) to compute Patlak slope and intercept images. Note that for many radiotracers beyond FDG, radioactive metabolites are present in the blood, and image-derived blood pool measurements may not accurately estimate the required PIF. Nonetheless, even using non-invasive estimation may be an improvement compared to existing SUV methodology (that simply assumes integral of PIF is proportional to injected dose divided by body weight), and use of population-based PIFs can help in better modeling of these effects, but this needs to be evaluated carefully.

There may be concerns about the validity of using population-based PIFs for estimation of a patient-specific PIF. For instance, let us consider DWB FDG imaging performed 50–80 min post-injection with six WB passes (~5 min/pass). We emphasize three important points:

- (1) Population-based PIFs are personalized in DWB imaging, since they can be scaled based on the later multi-time-point scans over the heart (and/or other blood pools) in each specific subject.
- (2) Only an estimate of the *integral* of PIF, and not actual PIF values, of the early times (before PET measurements are performed) are needed in Patlak analysis (see Eq. 1);

thus, there is less sensitivity to accuracy of individual PIF values at early times before PET imaging.

(3) Finally, and importantly, while the scaled population-based PIF approach is surely an approximation to the true PIF shape, conventional routinely-utilized SUV analysis makes *no* use of the input function at all, and as discussed for Eq. 4, it makes an even stronger approximation (namely of proportionality between the integral of the PIF and the injected dose divided by weight of the patient).

In any case, the impact of such a framework on test–retest repeatability of PET measures [101] remains to be carefully assessed.

### DWB acquisition protocols

Optimal acquisition times for different applications remain to be determined. A range of time windows have been considered and tried by different groups. In Table 1, we list a number of DWB protocols. The majority of these studies have involved FDG PET/CT, and the applicability of the technique for other tracers, particularly those with more complex kinetic properties, will require careful validation. The studies have involved either step-and-shoot (SS) or continuous bed motion (CBM), both of which accommodate DWB PET imaging. There also exist some efforts using PET/MRI (more on this later).

**Table 1** Listing of a number of DWB (multi-pass) PET protocols investigated or under investigation

Scan times* (minutes post-injection)	Acquisition protocol	Additional notes**
0–100	8 × 12 min/pass	PET/CT (SS) $^{18}\text{F}$ -FRP170; [103]
0–45	6 min single-bed (24 dynamic frames); DWB 6 × ~6 min/pass	PET/CT (SS) [59, 104, 105]
0–60	6 min single-bed (18 dynamic frames); DWB 6 × 9 min/pass	PET/CT (SS) [106]
0–90	6 min single-bed (24 frames); DWB 15 × 5 min/pass	PET/CT (SS) [81, 102, 107] PET/CT (CBM) [108]
0–60	3 min single-bed (15 frames); DWB (11–15) × ~4.5 min/pass	PET/CT (CBM) [83]
60–78	***DWB 4 × 4.5 min/pass or 6 × 3 min/pass	PET/CT (SS) [80, 82] PET/CT (CBM) [82, 108]
45–60	Six WB passes (6 × ~2.5 min/pass)	PET/CT (CBM) [83]
0–77	****6 min single-bed (20 frames) over suspected pathology; 17 WB passes (variable WB scan speeds)	PET/CT (CBM); initial scan over suspected pathology (instead of heart) [109, 110]
30–55	DWB 5 × 4.5 min/pass	PET/MRI [111]
0–90	6 min single-bed (24 dynamic frames); DWB 8 × 10.5 min/pass	PET/CT (SS) $^{68}\text{Ga}$ -DOTATOC [112]
0–60	10 min single-bed (26 frames); six WB passes (30s/bed with ten beds)	PET/MRI; PET active partially during MRI sequences [113]
0–95	*****6 min single-bed (nine frames); 19 WB passes (4 × 2 min/pass, 15 × 5 min/pass)	PET/CT (CBM)
50–80	DWB 6 × 5 min/pass	PET/CT (SS)

All studies are for FDG except when indicated otherwise.

\*These longer ( $\geq 90$  min) scans are used for new clinical applications and/or optimization of data acquisition (e.g., optimal imaging window; early vs late imaging) and are sometimes accompanied with arterial or venous blood sampling for validation purposes

\*\*All studies involve  $^{18}\text{F}$ -FDG PET except when indicated

\*\*\*This protocol is designed for a 60–78 min post-injection acquisition window matching that of some standard-of-care FDG WB PET exams

\*\*\*\*This protocol, due to initial scanning over a bed position containing suspected pathology, enables use of models beyond Patlak for that single bed, while allowing Patlak modeling for all the bed positions

\*\*\*\*\*The last two efforts (two rows) are under investigation at Yale, Geneva, and Johns Hopkins PET centers

The advantage of imaging immediately post-injection is to help obtain truly individual PIF estimates. Also imaging early has the advantage of capturing early tracer dynamics and producing better quantification in DWB [102]. Nonetheless, performing DWB imaging later (at or around 60–90 min post-injection) has the advantage of higher tracer accumulation in the target, which is why standard FDG SUV imaging is performed as such. Very importantly, such imaging can additionally produce estimates for conventional SUV imaging by summation of dynamic frames [80, 82], and as such, has a higher chance of more immediate translation to routine clinical imaging.

## Tackling noisy images

Dynamic imaging can result in the generation of images that are noisy, and which also in turn produce noisy parametric images (e.g., see Fig. 4a,c). This issue is accentuated in DWB where imaging of a particular region is performed for only a portion of the total acquisition time. There are a number of means to tackle this:

(i) *Optimized sampling*: For a fixed total duration, modifying the number of WB passes may make a difference in Patlak imaging [59], but the improvements are likely small and may be statistically insignificant as long as more than two passes are used to enable more accurate estimation of the PIF [114]. If the PIF is known, accurate estimates may be obtained from even two passes [78]. In any case, advanced optimization of sampling (including consideration of unequal durations per pass) as applied to different kinetic models might be worth pursuing [55].

(ii) *Improved statistical regression*: Kinetic parameter estimation, even when applied to simple models such as Patlak, can be enhanced by using advanced statistical modeling, including (i) weighting of frames by duration and/or counts for more appropriate weighted fitting, as well as (ii) using regularization, such as ridge regression or clustering-based methods, to reduce noise and variability in images [60, 115–119].

(iii) *4D image reconstruction*: Dynamic PET commonly involves independent reconstruction of dynamic frames. This can result in very noisy images that may challenge robust kinetic model fitting, and the reconstructed images may also contain noise-induced bias in low-uptake regions (due to the

non-negativity constraint in the OSEM reconstruction algorithm) [120]. Furthermore, accurate kinetic parameter estimation requires modeling of the noise distribution in the reconstructed images (noise covariance matrix), which can be difficult and time-consuming to compute [121, 122]. In fact, space-variant noise variance and inter-voxel correlations are often neglected in routine kinetic modeling. An alternative approach is to directly estimate the kinetic parameters from dynamic sinogram data (see reviews [123–125]). This is done by (i) processing the dynamic sinograms into a single sinogram followed by a single reconstruction [126–128], or (ii) by use of more advanced 4D statistical models [129–134] which have the advantage of accurately modeling Poisson noise distributions in the data space. These approaches to create parametric images directly from sinogram data are applicable to or were already explored for Patlak imaging in the past, and in more recent years for whole-body Patlak imaging [78, 104, 107]. This included ‘nesting’ the Patlak model within the iterative reconstruction framework for accelerated convergence [104] using optimization transfer principles [135]. In Fig. 4, we show examples (30 min DWB acquisition time windows) demonstrating that significantly improved images are produced using the direct approach, compared to conventional indirect parametric image generation. In fact, there is now a vendor product (FlowMotion™ Multiparametric PET by Siemens) that implements the accelerated (nested) direct Patlak reconstruction methodology [135].

### Non-compartmental analysis of DWB PET data

DWB images can play a key role in new imaging applications which perform more thorough assessments of the time course of radiotracer uptake [103]. It is also possible to use non-compartmental methods to combine the generated DWB images to create parametric images. An example is the use of principal

component analysis (PCA) [136] which explains the variance-covariance structure in a dynamic dataset using a series of linear combinations of the original variables, and can be applied in our case to the measured TACs at the voxel level. Such an approach is data-driven in the sense that it makes no assumptions about the underlying tracer kinetics and requires no PIF. PCA has been previously used in the context of dynamic PET at a single bed-position for improved detection of different signals and regions present in the images [137–140]. Data shown in Fig. 5 illustrate an example application to DWB FDG PET. In these data, the principal component 1 (PC1) image was found to resemble a low-noise summation image, whereas the PC2 image was weighted towards increasing TACs, including tumors. However, one must be cautious that in some studies, components may not be fully separated, leading to problems especially for quantitative applications. Alternatively, it is possible to apply other non-compartmental methods to dynamic images and TACs such as independent component analysis (ICA) [141, 142], factor analysis [143–146], spectral analysis [147, 148], cluster analysis [149] or heterogeneity analysis (e.g., fractal dimension) [38]. It remains to be demonstrated whether these methods, given their subtleties and challenges (such as the challenge of accurately mapping their derived images to specific physiological processes) will translate to clinical applications.

### Clinical potential

#### Assessment of systemic disease

DWB PET is an enabling technology with promising clinical potential. Specifically, there is significant potential for improved quantification and assessment of systemic disease, including cancer, inflammation and infection. Overall, dynamic imaging and parametrization enable more accurate

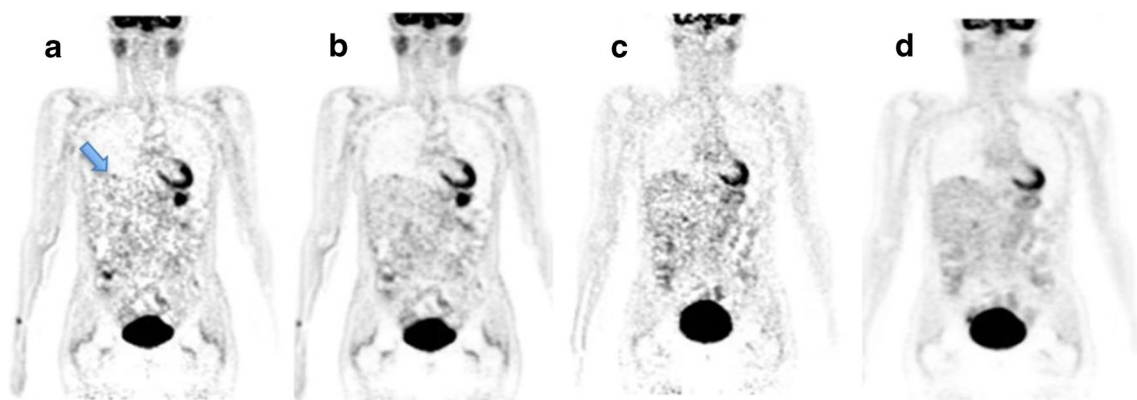


**Fig. 4** Parametric images for 30 min ( $6 \times 5$  min/pass) time windows. **a** Indirect  $K_i$  and **b** direct  $K_i$  images for frames spanning ~10–40 min post-injection. **c** Indirect  $K_i$  and **d** direct  $K_i$  images for frames spanning ~60–90 min post-injection. Three iterations (21 subsets) were used, and 6 mm

Gaussian filter post-smoothing was performed. The small tumor (shown by arrow) at the dome of the liver is seen in early imaging (**a**, **b**) but only on direct  $K_i$  image for later imaging (**d**)



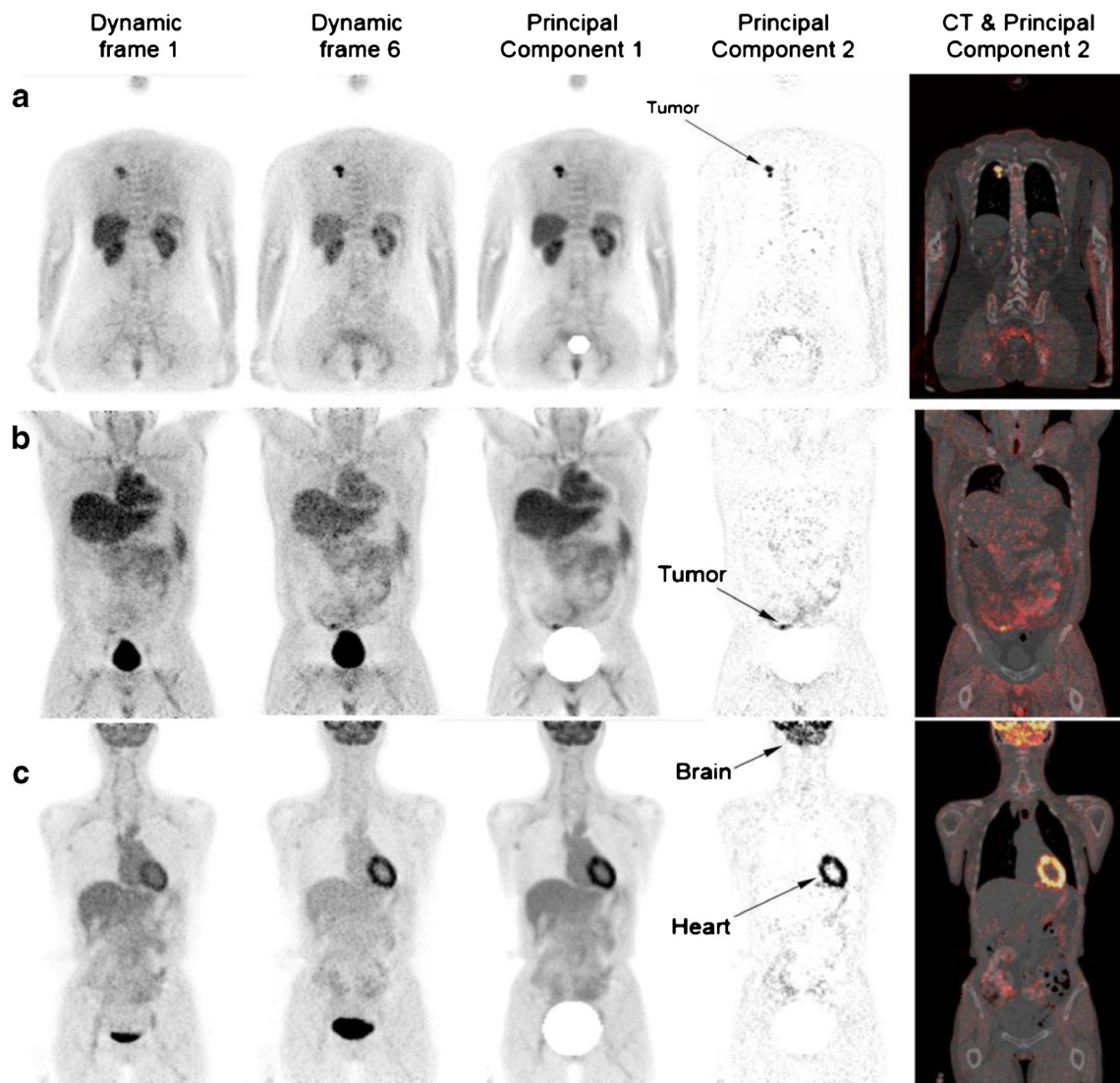


**Fig. 5** Three patient examples showing how PCA could potentially be used to aid assessment of dynamic FDG studies. Each study involved six dynamic frames. The bladder was suppressed prior to PCA analysis.

Patients A and B had tumors in lung and pelvis respectively, while patient C had a normal FDG distribution. Note the high contrast seen in PCA component 2 (column 4), reflecting the increasing FDG uptake

quantification of uptake, which may be of special significance for improved diagnosis as well as monitoring of therapy response [150]. In the latter, alterations in background physiologic uptake or in the PIF following treatment may confuse therapy assessment in conventional SUV imaging [11]. In addition, it is expected that quantitative results derived from the DWB imaging procedure will be less time-dependent than single-time-point static SUV whole body images.

We also envision the DWB methodology to be of value in experimental treatments (including phase 1 clinical trials), where patients with systematic disease (e.g., metastatic burden) undergo imaging and treatment. In such studies, WB imaging has high significance, and transition to DWB imaging can retain advantages of WB assessment while providing improved quantification of disease.

DWB imaging may also add value to clinical trials wherein tracers beyond FDG are utilized, aiming to capture and quantify different aspects of disease than FDG does. This includes radiotracers for which SUV is not reliable or fully informative. An example includes PET imaging with tyrosine kinase inhibitors (TKIs) [151]. As another example, consider  $^{68}\text{Ga}$ -DOTATOC PET/CT for imaging neuroendocrine tumors (NET). Dynamic  $^{68}\text{Ga}$ -DOTATOC PET has been suggested as the preferred acquisition mode over conventional static SUV PET, which may not reflect somatostatin receptor density accurately at higher values [74]. At the same time, metastatic NETs can extend well beyond the axial range of a single PET bed position. Accommodating both these considerations, Fig. 6 provides evidence of the feasibility of DWB  $^{68}\text{Ga}$ -DOTATOC PET/CT, involving acquisition of dynamic PET



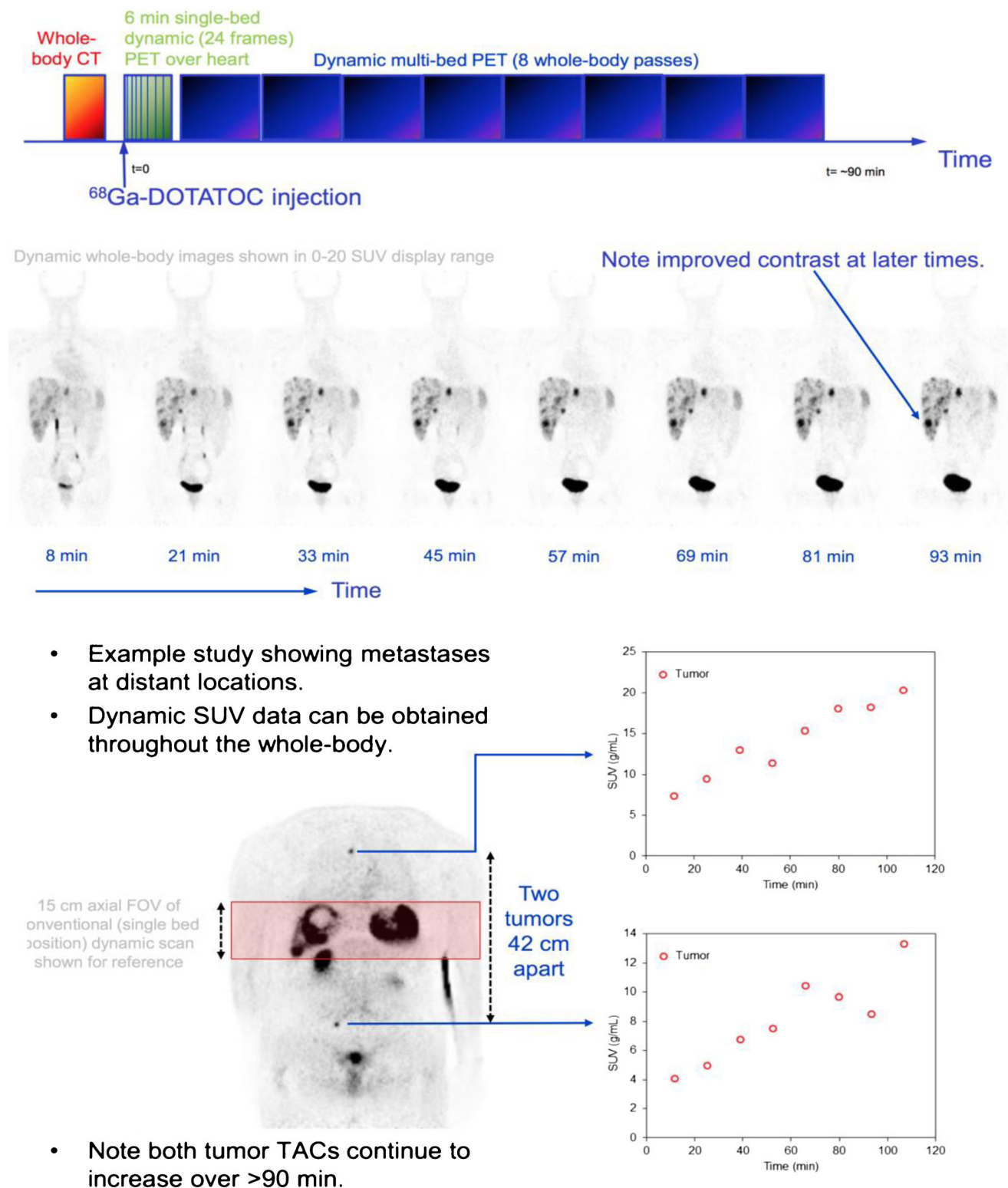


**Fig. 6** An example of DWB  $^{68}\text{Ga}$ -DOTATOC PET/CT imaging. The protocol involved WB (eyes to mid-thigh) low-dose CT and  $^{68}\text{Ga}$ -DOTATOC injection simultaneous with the start of a 6 min, single-bed, dynamic PET over the heart, immediately followed by eight sequential WB PET scans ( $8 \times 7$  bed positions  $\times$  1.5 min / bed). TACs increased throughout the ~90 min imaging period. The initial dynamic series over

the heart and negligible myocardial uptake in the WB images suggest potential for non-invasive image-derived PIF determination, although this capability needs to be carefully validated. In this dynamic imaging protocol, the extended scan range enabled by the DWB technique revealed unexpected metastases in the thoracic vertebrae

data over an extended axial range. Overall, DWB provides potentials for improved assessment of disseminated disease.

### Study of systemic interactions and responses

The ability for DWB to quantify multiple organs throughout the body opens up new opportunities for imaging. An area of significant potential is study of the gut–brain axis. This is related to findings that bacteria in the gastrointestinal (GI) tract have the ability to activate neural pathways and central nervous system (CNS) signaling systems [152]. For instance, there are emerging models of Parkinson’s disease in which misfolded  $\alpha$ -synuclein proteins could propagate from the gut epithelium to the brain [153, 154]. Another example is the study of the heart–brain axis, whereby the cardiovascular and nervous systems interact in complex ways and in both directions [155]. An interesting recent PET study on mice, for instance, revealed the brain to be susceptible to acute myocardial infarction and chronic heart failure, potentially inducing neuroinflammation as a precursor to neurodegeneration [156]. In a patient study of stress-induced atherosclerosis, regional brain FDG PET activity in the amygdala was associated with arterial inflammation as measured using FDG, and significantly predicted subsequent cardiovascular disease events [157]. Such studies have significant implications and may be performed on humans via the DWB framework to provide a wider set of multi-parametric and co-registered molecular images.

### Application to PET/MRI imaging

Combined PET/MRI instrumentation has the potential to provide more than merely a radiation-free anatomical context for PET imaging [158–161]. Although the optimum way to deploy the technology is still under development, a range of different MR sequences enabling multiparametric MR imaging are available, including T1-, T2-, diffusion-weighted and dynamic contrast-enhanced MR imaging [162]. Whereas much PET/CT protocol development has been aimed at reducing PET acquisition times [163], with simultaneous PET/MRI, overall scan durations are expected (and accepted) to be longer to enable multiple MR sequences and to provide a wealth of information that can potentially complement the PET data. This increased time provides a great opportunity for DWB PET. The complementary MR imaging capability may also enable enhanced PIF estimation, motion correction, and synergistic kinetic modeling [164, 165].

An example application of DWB is shown in Fig. 7, involving Patlak analysis fit to a population-based PIF scaled to the individual patient, given late samples from the left ventricular blood pool. Given MR images, motion data between different passes were extracted using the non-rigid registration method [111]. Recently, Johansson et al. [113] used DWB

PET/MR imaging to perform simultaneous WB assessment of tissue-specific insulin-mediated FDG influx rates via PET, and tissue depots by MR. Results indicate that DWB FDG PET/MR is feasible. Additionally, the MRI protocol may be expanded to perform additional imaging sequences as well as use of different MR image contrasts.

### “Black-blood PET” imaging?

Another application that might aptly fit within the DWB framework is WB imaging of vessel wall inflammation. Multiple studies have demonstrated the value of FDG PET/CT for detecting active inflammation in vessel wall [166, 167]. In atherosclerosis, which is a chronic inflammatory response to lipid accumulation in the artery wall, the artery plaques are clinically silent for years. Vulnerable plaques that fissure or erode to trigger thrombus formation and cause acute ischemia are the ones that cause dramatic clinical manifestations. Resident macrophages in plaques show higher metabolic trapping of FDG than the neighboring cells. FDG PET imaging is typically performed 2 h or more post-injection, to minimize blood pool activity and to increase the target-to-background ratio in the walls. The DWB framework poses a potential, alternative way of inspecting FDG uptake at earlier times. The methodology is analogous to black-blood MRI imaging [168, 169], where the blood signal in the vessel lumen is saturated, while signal in the vessel walls is visualized. Similarly, since Patlak images show the rate of uptake in the region of interest, tracer activity in blood will be saturated, potentially enabling assessment of inflammation in the walls of major vessels [170]. Such a framework needs to be carefully assessed and verified, as the imaging of small structures such as the blood vessel wall may be very sensitive to patient motion artifacts.

## Additional considerations

### Towards parametric PET imaging in the clinic

Dynamic PET acquisition enabling quantitative imaging is well established in the research setting, but has not been widely adopted in routine clinical imaging. Neurological PET, by contrast, has witnessed a proliferation of dynamic quantitative techniques. This is related to the observation that the vast majority of neuro PET tracers do not have sufficient sensitivity and specificity for diagnostic or prognostic purposes (e.g., see [171]), leading to investigation of quantitative parameter estimation techniques to enhance the study of subtle task- or disease-induced neurological alterations. By contrast, given the successful clinical adoption of tracers such as FDG in oncologic PET imaging, substantially less work has been devoted to quantitative methods in the clinic.

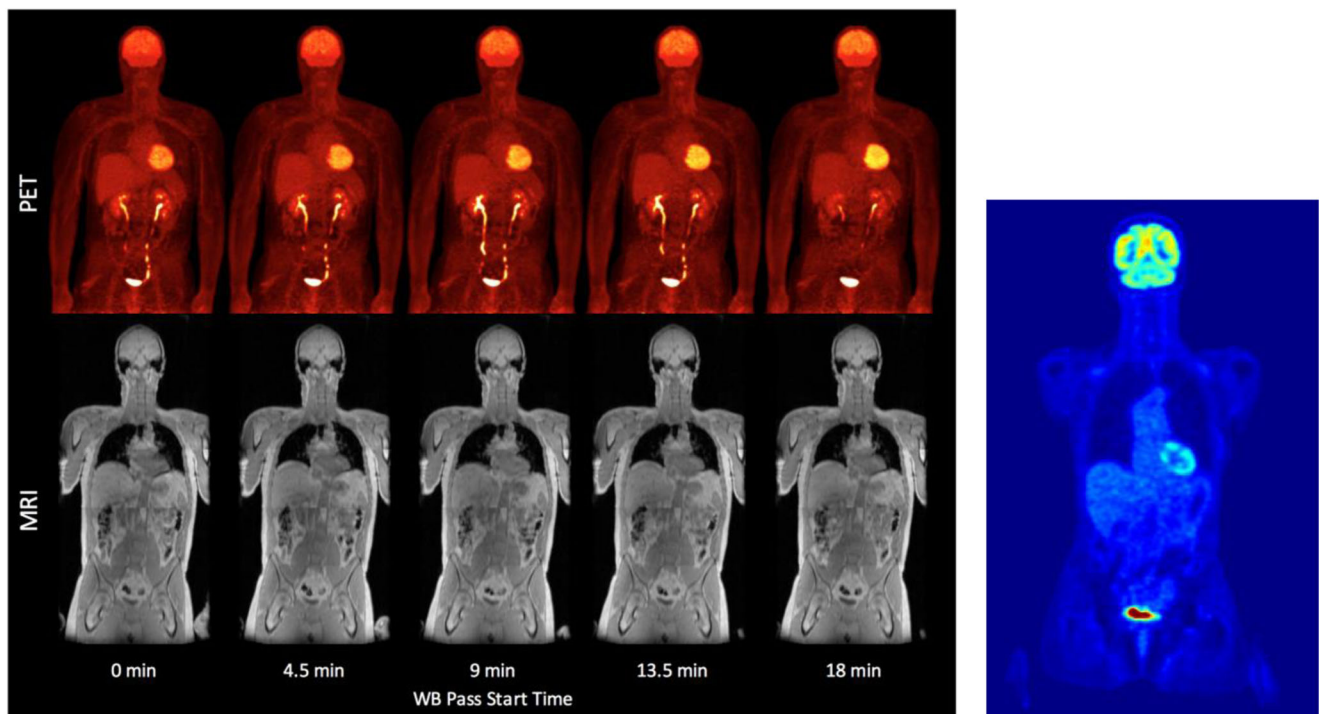


**Fig. 7** DWB applied to simultaneous FDG PET/MRI imaging. Motion correction was performed on MRI images (using automated B-spline image registration with normalized cross correlation as a cost function), and subsequently applied to PET images. The patient shown was imaged at 30–55 min post-injection of FDG (times shown above are with respect

to scan start time 30 min post-injection). DWB PET/MR consisted of five beds (stations) per WB pass and a total of 5 WB passes (scan time of 40 s/station). The time to complete each WB (head-through-thighs) scan and to begin another WB pass was approximately 4.5 min. The resulting parametric Patlak Ki image is shown on the *right*

At the same time, routine clinical PET imaging may significantly benefit from translation of quantitative methods to its domain to tackle the aforementioned limitations with conventional SUV imaging. Given the importance of WB PET coverage for clinical applications [41–45], the extension of dynamic PET protocols to multi-bed fields-of-view through DWB PET appears necessary for routine and wide adoption of parametric PET imaging. The combination of dynamic and WB PET imaging is very feasible, and parametric images may also be conveniently generated, as additionally evidenced by the availability of at least one vendor product supporting such a framework (FlowMotion™ Multiparametric PET by Siemens Healthineers). The DWB framework remains to be employed in a wide setting to identify in which areas it can add significant value to clinical imaging. An important consideration, in order to more readily enable routine clinical adoption of DWB PET, is to perform a single multi-bed DWB PET acquisition from which PET images comparable to current standard-of-care whole-body PET SUV images are generated, while also providing parametric PET images to improve diagnosis and clinical interpretation. This, as we have indicated in the above discussions, is quite feasible.

An alternative approach is to build PET scanners with very large axial coverage of the human body, such as the proposed total-body EXPLORER system [172]. This exciting technology, which is in its developmental stages, would readily

enable dynamic WB imaging, with advantages of significantly increased sensitivity (by a factor of 40 for WB imaging using a 2 m-long total-body system) and continuous temporal coverage across the body (enabling application of a wider range of compartmental kinetic modeling methods). At the same time, while total-body systems can significantly shorten routine PET scans given the sensitivity boost, duration of dynamic imaging can probably not be significantly shortened given the time needed for redistribution of radiopharmaceuticals. Overall, it remains to be seen to what extent such systems will be available and employed in the future. By contrast, the DWB framework is readily employable in PET imaging today.

### Pitfalls

There are a number of pitfalls in DWB imaging. Routine single-pass WB imaging limits imaging of each bed to a single contiguous block of time. By contrast, in DWB each bed position is visited multiple times. This can increase chances of organ movement or overall body motion in between the passes. On one occasion, for instance, we observed a lesion in the bladder, visible in the conventional SUV image, disappear in DWB Patlak imaging. This was found to be related to expansion of the bladder in the course of the scan and an inconsistent lesion location. In addition, direct 4D parametric

imaging poses enhanced sensitivity to subject motion [173]. As for outward patient movements, it is our experience that a well-trained team of technologists can help significantly minimize such issues with cooperative patients. It may also be worth exploring the use of inflatable individually molded cushions [174]. Finally, it is worth exploring motion-correction methods if notable motion occurs. An example of this was achieved in Fig. 7 in the context of PET/MRI imaging.

Another limitation is related to the fact that routine clinical PET scans are nowadays performed with increasingly shorter durations (< 20 min for WB imaging). These typically involve the use of six to seven beds with 2–3 min/bed, given the impressive performance of new-generation PET scanners. However, to properly capture reasonable kinetics in tracer redistribution, ~30 min (or possibly more time) may be required. This issue remains to be carefully assessed. With the availability of DWB as an enabling technology, it remains to be shown whether significantly improved clinical task performance can be obtained, taking into account the economics of PET imaging as well a busy working clinic.

We also note that standard Patlak analysis is based on assumption of irreversible kinetics (e.g., in Fig. 2,  $k_4$  is assumed negligible). This may not be an entirely correct assumption for FDG (see references and discussion in [105]), leading to underestimation of the Patlak slope if imaging is performed at later times [102]. Solutions to this include use of pre-determined  $k_4$  values [115], or the generalized Patlak model that takes this reversibility into account and estimates it. The latter maintains advantages of Patlak imaging (not requiring early or continuous PET imaging), while providing more accurate quantitation [105]. Nonetheless, it results in a greater number of noisy images due to the added complexity of the model. This may in part be tackled by direct 4D parametric imaging [104]. Furthermore, an approach has been to perform early imaging over a single bed position covering suspected pathology, followed by multi-pass WB imaging. In this case, it is possible to employ more elaborate compartmental kinetic models (estimating the individual rate constants) for the particular bed position, while performing Patlak imaging for all imaged WB bed positions [109].

We also note that standard FDG Patlak modeling may be especially inaccurate for certain organs. In particular, liver is better modeled by a dual-input kinetic model, given the dual blood supply from the hepatic artery and the portal vein [175], and kidney involves very complex kinetics [176]. At the same time, SUV modeling also neglects such complex models, in fact to an even larger extent than standard Patlak analysis. In the case of the liver, for instance, Patlak analysis is actually applicable [175] but greater accuracy is gained by having a modified PIF as applied to the model.

## Summary of advantages

DWB imaging has a number of potential advantages that are of interest:

- 1) It combines the abilities to visualize and quantify radio-tracer uptake across the body, enabling opportunities for improved imaging and quantification of systemic disease as well as systemic interactions and responses.
- 2) It can minimize time dependence of SUV activity: SUV uptake (Eq. 4) changes in time in direct proportion to changes in image uptake. Given variable scan times inherent in a busy clinical practice, this is an issue, and the proposed measures may be less subject to such alterations in exact acquisition times.
- 3) It can remove background uptake, allowing small and less FDG avid tumors to be identified. This is in contrast to the “sea of background” situation in conventional single-pass SUV imaging. This may be particularly helpful in the upper abdomen, especially the liver.
- 4) The parametric values may go to “zero”, unlike background activity in traditional PET imaging, resulting in a larger dynamic range for PET.
- 5) Images with improved quantification may be obtained with significantly less wait-time in some settings (e.g., in comparison to dual-time-point imaging).
- 6) For certain DWB acquisition protocols, conventional SUV images are readily obtained by summation of multiple passes through the subject, while also providing multiple parametric images. Overall, a single imaging session can be used to generate complementary images while retaining benefits of conventional SUV imaging.

## Challenges to wide usage

There are a number of challenges to wide usage of DWB PET. The most important one appears to be additional scanning time required (cost and logistics). PET imaging centers are moving towards increasingly shorter scan durations. While 30 min imaging was routine in previous years, with new generation PET scanners, WB imaging with total times less than 20 min is becoming more routine. This poses a challenge to DWB PET imaging, which will probably require longer scan times. It remains to be determined by our community when the trade-off is justified, as applications for DWB PET are more extensively evaluated. A practical idea proposed (by Dr. Rich Carson) has been to employ DWB PET imaging for the first patient of the day, which does not incur additional cost, in the sense that instead of waiting in the uptake room, part or all of that time is spent on the scanner, to accumulate sufficient data and evidence for new applications.



Another challenge to wider usage of DWB PET is the perception that population-based PIF estimation methods can bring about significant lack of accuracy. What we have emphasized in this work is that the prevalent SUV quantitation framework makes an even more simplistic approximation for the PIF, thus suffering from greater inaccuracy. Nonetheless, it does remain to be seen whether the DWB PET methodology results in significantly increased variability (reduced precision). This is also related to the fact that kinetic modeling (even linear regression in Patlak) within DWB PET can result in noisier (and less reproducible) images. This potential trade-off between increased quantitative accuracy and reduced precision will need to be carefully assessed for different clinical applications.

## Conclusion

DWB PET is a powerful imaging framework that enables improved visualization of specific tracer uptake vs background uptake, and may produce more accurate quantitative measures of disease. It can be employed to complement conventional whole-body SUV images with other highly quantitative parametric images, such as that of influx rate of uptake. Given the impressive performance of current-generation clinical PET scanners, DWB PET imaging appears fully feasible and has the potential to add significant value to clinical imaging and clinical research.

**Acknowledgements** This work was in part supported by Siemens Medical Solutions, and by the Swiss National Science Foundation under Grant SNSF 320030\_176052. We wish to gratefully acknowledge valuable discussions and/or support from Corina Voicu, Ramya Rajaram, Darrell Burckhardt, Bernard Bendriem, Saeed Ashrafinia, Jeff Leal, Joo O, Fotis Kotasidis, Rathana Subramaniam, Lilja Solnes, Hyungseok Jang, Hyung-Jun Im, Mika Naganawa, Richard Carson, Harvey Ziessman, Albert Gjedde and Simon Cherry.

**Funding** This study was in part funded by Siemens Medical Solutions, and by the Swiss National Science Foundation under Grant SNSF 320030\_176052.

## Compliance with ethical standards

**Conflict of interest** Authors Arman Rahmim, Nicolas A. Karakatsanis, Habib Zaidi and Richard L. Wahl have received research support from Siemens Medical Solutions, and authors Alan McMillan and Steve Cho have received research support from GE Healthcare. Authors Martin A. Lodge and Yun Zhou declare that they have no conflict of interest. Vladimir Panin and Michael Casey are employees of Siemens Healthineers.

**Ethical approval** All procedures performed in studies involving human participants were in accordance with the ethical standards of the institutional and/or national research committee and with the 1964 Helsinki Declaration and its later amendments or comparable ethical standards.

**Informed consent** Informed consent was obtained from all individual participants included in the study.

## References

1. Wahl RL, Buchanan JW. Principles and practice of positron emission tomography. Philadelphia, PA: Lippincott Williams & Wilkins; 2002.
2. Shreve PD, Anzai Y, Wahl RL. Pitfalls in oncologic diagnosis with FDG PET imaging: physiologic and benign variants. *Radiographics*. 1999;19:61–77.
3. Zasadny KR, Wahl RL. Standardized uptake values of normal tissues at PET with 2-[fluorine-18]-fluoro-2-deoxy-D-glucose: variations with body weight and a method for correction. *Radiology*. 1993;189:847–50.
4. Wahl RL, Quint LE, Cieslak RD, Aisen AM, Koeppe RA, Meyer CR. Anatomic metabolic tumor imaging — fusion of FDG PET with CT or MRI to localize foci of increased activity. *J Nucl Med*. 1993;34:1190–7.
5. Wahl RL, Quint LE, Orringer M, Meyer CH. Staging non-small-cell lung cancer in the mediastinum — comparison of FDG-PET, CT and hybrid anatomic metabolic fusion images with pathology. *Radiology*. 1992;185:324.
6. Mawlawi O, Townsend DW. Multimodality imaging: an update on PET/CT technology. *Eur J Nucl Med Mol Imaging*. 2009;36: 15–29. <https://doi.org/10.1007/S00259-008-1016-6>.
7. Delso G, Furst S, Jakoby B, Ladebeck R, Ganter C, Nekolla SG, et al. Performance measurements of the Siemens mMR integrated whole-body PET/MR scanner. *J Nucl Med*. 2011;52:1914–22. <https://doi.org/10.2967/Jnumed.111.092726>.
8. Wehrli HF, Sauter AW, Judenhofer MS, Pichler BJ. Combined PET/MR imaging — technology and applications. *Technol Cancer Res Treat*. 2010;9:5–20.
9. Hamberg LM, Hunter GJ, Alpert NM, Choi NC, Babich JW, Fischman AJ. The dose uptake ratio as an index of glucose metabolism: useful parameter or oversimplification? *J Nucl Med*. 1994;35:1308–12.
10. Keyes JW Jr. SUV: standard uptake or silly useless value? *J Nucl Med*. 1995;36:1836–9.
11. Huang S-C. Anatomy of SUV. *Nucl Med Biol*. 2000;27:643–6.
12. Adams MC, Turkington TG, Wilson JM, Wong TZ. A systematic review of the factors affecting accuracy of SUV measurements. *AJR Am J Roentgenol*. 2010;195:310–20.
13. Strauss LG. Fluorine-18 deoxyglucose and false-positive results: a major problem in the diagnostics of oncological patients. *Eur J Nucl Med Mol Imaging*. 1996;23:1409–15.
14. Lodge MA, Lucas JD, Marsden PK, Cronin BF, O'Doherty MJ, Smith MA. A PET study of 18FDG uptake in soft tissue masses. *Eur J Nucl Med Mol Imaging*. 1999;26:22–30.
15. Freedman TNM, Sundaram KS, Kurdziel K, et al. Comparison of SUV and Patlak slope for monitoring of cancer therapy using serial PET scans. *Eur J Nucl Med Mol Imaging*. 2003;30:8.
16. Zaidi H, Karakatsanis N. Towards enhanced PET quantification in clinical oncology. *Br J Radiol*. 2017;91:20170508.
17. Sugawara Y, Zasadny KR, Grossman HB, Francis IR, Clarke MF, Wahl RL. Germ cell tumor: differentiation of viable tumor, mature teratoma, and necrotic tissue with FDG PET and kinetic modeling. *Radiology*. 1999;211:249–56.
18. Zasadny KR, Wahl RL. Enhanced FDG-PET tumor imaging with correlation-coefficient filtered influx-constant images. *J Nucl Med*. 1996;37:371–4.
19. Chan WL, Ramsay SC, Szeto ER, Freund J, Pohlen JM, Tarlinton LC, et al. Dual-time-point (18)F-FDG-PET/CT imaging in the assessment of suspected malignancy. *J Med Imag Radiat*. 2011;55:379–90. <https://doi.org/10.1111/J.1754-9485.2011.02287.X>.
20. Freeman LM, Johnson PM. Clinical radionuclide imaging. 3rd Ed. Orlando FL, Grune & Stratton Inc.; 1984.

21. Weissman BN. Imaging of arthritis and metabolic bone disease. Philadelphia PA: Elsevier Health Sciences; 2009.
22. Gullberg GT, Reutter BW, Sitek A, Maltz JS, Budinger TF. Dynamic single photon emission computed tomography—basic principles and cardiac applications. *Phys Med Biol*. 2010;55: R111.
23. Imbert L, Poussier S, Franken PR, Songy B, Verger A, Morel O, et al. Compared performance of high-sensitivity cameras dedicated to myocardial perfusion SPECT: a comprehensive analysis of phantom and human images. *J Nucl Med*. 2012;53:1897.
24. Nesterov SV, Deshayes E, Sciagrà R, Settimo L, Declerck JM, Pan X-B, et al. Quantification of myocardial blood flow in absolute terms using (82)rb PET imaging: the Ruby-10 Study. *JACC Cardiovasc Imaging*. 2014;7:1119–27.
25. Dunnwald LK, Doot RK, Specht JM, Gralow JR, Ellis GK, Livingston RB, et al. Pet tumor metabolism in locally advanced breast cancer patients undergoing neoadjuvant chemotherapy: value of static versus kinetic measures of fluorodeoxyglucose uptake. *Clin Cancer Res*. 2011;17:2400–9. <https://doi.org/10.1158/1078-0432.Ccr-10-2649>.
26. Tomasi G, Turkheimer F, Aboagye E. Importance of quantification for the analysis of pet data in oncology: review of current methods and trends for the future. *Mol Imaging Biol* 2012;14(2): 131–46.
27. Lodge MA, Badawi RD, Gilbert R, Dibos PE, Line BR. Comparison of 2-dimensional and 3-dimensional acquisition for (18)F-FDG PET oncology studies performed on an LSO-based scanner. *J Nucl Med*. 2006;47:23–31.
28. Allen-Auerbach M, Weber WA. Measuring response with FDG PET: methodological aspects. *Oncologist*. 2009;14:369–77. <https://doi.org/10.1634/Theoncologist.2008-0119>.
29. Leskinen-Kallio S, Nagren K, Lehtikainen P, Ruotsalainen U, Teras M, Joensuu H. Carbon-11-methionine and PET is an effective method to image head and neck cancer. *J Nucl Med*. 1992;33: 691–5.
30. Liu P, Huang G, Dong S, Wan L. Kinetic analysis of experimental rabbit tumour and inflammation model with 18f-FDG PET/CT. *Nuklearmedizin*. 2009;48:153–8.
31. Sundaram SK, Freedman NM, Carrasquillo JA, Carson JM, Whatley M, Libutti SK, et al. Simplified kinetic analysis of tumor 18f-FDG uptake: a dynamic approach. *J Nucl Med*. 2004;45: 1328–33.
32. Strauss LG, Klippel S, Pan L, Schonleben K, Haberkorn U, Dimitrakopoulou-Strauss A. Assessment of quantitative FDG PET data in primary colorectal tumours: which parameters are important with respect to tumour detection? *Euro J Nucl Med Mol Imaging*. 2007;34:868–77.
33. Song SL, Deng C, Wen LF, Liu JJ, Wang H, Feng D, et al. 18f-FDG PET/CT-related metabolic parameters and their value in early prediction of chemotherapy response in a VX2 tumor model. *Nucl Med Biol*. 2010;37:327–33.
34. Okazumi S, Dimitrakopoulou-Strauss A, Schwarzbach MH, Strauss LG. Quantitative, dynamic 18f-FDG-PET for the evaluation of soft tissue sarcomas: relation to differential diagnosis, tumor grading and prediction of prognosis. *Hellj Nucl Med*. 2009;12:223–8.
35. Krak NC, Van Der Hoeven JJ, Hoekstra OS, Twisk JW, Van Der Wall E, Lammertsma AA. Measuring [(18)F]FDG uptake in breast cancer during chemotherapy: comparison of analytical methods. *Euro J Nucl Med Mol Imaging*. 2003;30:674–81.
36. Graham MM, Peterson LM, Hayward RM. Comparison of simplified quantitative analyses of FDG uptake. *Nucl Med Biol*. 2000;27:647–55.
37. Freedman NM, Sundaram SK, Kurdziel K, Carrasquillo JA, Whatley M, Carson JM, et al. Comparison of SUV and Patlak slope for monitoring of cancer therapy using serial PET scans. *Euro J Nucl Med Mol Imaging*. 2003;30:46–53.
38. Dimitrakopoulou-Strauss A, Strauss LG, Heichel T, Wu H, Burger C, Bernd L, et al. The role of quantitative (18)F-FDG PET studies for the differentiation of malignant and benign bone lesions. *J Nucl Med*. 2002;43:510–8.
39. Young H, Baum R, Cremerius U, Herholz K, Hoekstra O, Lammertsma AA, et al. Measurement of clinical and subclinical tumour response using [F-18]-fluorodeoxyglucose and positron emission tomography: review and 1999 EORTC recommendations. *Eur J Cancer*. 1999;35:1773–82.
40. Weber WA, Ziegler SI, Thodtmann R, Hanauske A-R, Schwaiger M. Reproducibility of metabolic measurements in malignant tumors using FDG PET. *J Nucl Med*. 1999;40:1771–7.
41. Dahlbom M, Hoffman EJ, Hoh CK, Schiepers C, Rosenqvist G, Hawkins RA, et al. Whole-body positron emission tomography: part I. Methods and performance characteristics. *J Nucl Med*. 1992;33:1191–1199.
42. Hustinx R, Bènard F, Alavi A. Whole-body FDG-PET imaging in the management of patients with cancer. *Sem Nucl Med*. 2002;32: 35–46.
43. Kubota K, Itoh M, Ozaki K, Ono S, Tashiro M, Yamaguchi K, et al. Advantage of delayed whole-body FDG-PET imaging for tumour detection. *Eur J Nucl Med Mol Imaging*. 2001;28:696–703.
44. Townsend DW. Positron emission tomography/computed tomography. *Sem Nucl Med*. 2008;38:152–66.
45. Boellaard R, O'doherty MJ, Weber WA, Mottaghy FM, Lonsdale MN, Stroobants SG, et al. FDG PET and PET/CT: EANM procedure guidelines for tumour PET imaging: version 1.0. *Eur J Nucl Med Mol Imaging*. 2010;37:181–200. <https://doi.org/10.1007/S00259-009-1297-4>.
46. Karp JS, Surti S, Daube-Witherspoon ME, Muehllehner G. Benefit of time-of-flight in PET: experimental and clinical results. *J Nucl Med*. 2008;49:462–70. <https://doi.org/10.2967/Jnumed.107.044834>.
47. Surti S. Update on time-of-flight PET imaging. *J Nucl Med*. 2015;56:98–105. <https://doi.org/10.2967/Jnumed.114.145029>.
48. Kadmas DJ, Casey ME, Conti M, Jakoby BW, Lois C, Townsend DW. Impact of time-of-flight on PET tumor detection. *J Nucl Med*. 2009;50:1315–23. <https://doi.org/10.2967/Jnumed.109.063016>.
49. Cherry SR, Sorenson JA, Phelps ME. Physics in nuclear medicine. 4th ed. Philadelphia, PA: Elsevier Saunders; 2012.
50. Chandra R, Rahmim A. Nuclear medicine physics: the basics. 8th ed. Philadelphia, PA: Wolters Kluwer; 2017.
51. Armstrong IS, James JM, Williams HA, Kelly MD, Matthews JC. The assessment of time-of-flight on image quality and quantification with reduced administered activity and scan times in 18f-FDG PET. *Nucl Med Commun*. 2015;36:728–37.
52. Kadmas DJ, Oktay MB, Casey ME, Hamill JJ. Effect of scan time on oncologic lesion detection in whole-body PET. *IEEE Trans Nucl Sci*. 2012;59:1940–7.
53. Hutton BF. Recent advances in iterative reconstruction for clinical SPECT/PET and CT. *Acta Oncol*. 2011;50:851–8. <https://doi.org/10.3109/0284186x.2011.580001>.
54. Yang DC, Ratani RS, Mittal PK, Chua RS, Patel SM. Radionuclide three-phase whole-body bone imaging. *Clin Nucl Med*. 2002;27:419–26.
55. Ho-Shon K, Feng D, Hawkins R, Meikle S, Fulham M, Li X. Optimized sampling and parameter estimation for quantification in whole body PET. *IEEE Trans Biomed Eng*. 1996;43:1021–8.
56. Hoh CK, Levin CS, Vera DR. Whole body Patlak imaging. *J Nucl Med*. 2003;44:61.
57. Ng JM, Azuma K, Kelley C, Pencek R, Radikova Z, Laymon C, et al. Pet imaging reveals distinctive roles for different regional

- adipose tissue depots in systemic glucose metabolism in nonobese humans. *Am J Physiol-Endocrinol Metab.* 2012;303:E1134–E41.
58. Karakatsanis N, Lodge MA, Zhou Y, Mhlange J, Chaudhry MA, Tahari AK, et al. Dynamic multi-bed FDG PET imaging: feasibility and optimization. *IEEE Nucl Sci Symp Conf Theatr Rec.* 2011; 3863–70.
  59. Karakatsanis NA, Lodge MA, Tahari AK, Zhou Y, Wahl RL, Rahmim A. Dynamic whole body PET parametric imaging: I. concept, acquisition protocol optimization and clinical application. *Phys Med Bio.* 2013;58:7391–418.
  60. Karakatsanis NA, Lodge MA, Zhou Y, Wahl RL, Rahmim A. Dynamic whole body PET parametric imaging: II. task-oriented statistical estimation. *Phys Med Bio.* 2013;58:7419–45.
  61. Patlak CS, Blasberg RG, Fenstermacher JD. Graphical evaluation of blood-to-brain transfer constants from multiple-time uptake data. *J Cereb Blood Flow Metab.* 1983;3:1–7.
  62. Patlak CS, Blasberg RG. Graphical evaluation of blood-to-brain transfer constants from multiple-time uptake data. *Gener J Cereb Blood Flow Metab.* 1985;5:584–90.
  63. Gjedde A. High- and low-affinity transport of D-glucose from blood to brain. *J Neurochem.* 1981;36:1463–71.
  64. Gjedde A. Calculation of cerebral glucose phosphorylation from brain uptake of glucose analogs in vivo: a re-examination. *Brain Res Rev.* 1982;4:237–74.
  65. Rutland M. A single injection technique for subtraction of blood background in 131I-hippuran renograms. *Br J Radiol.* 1979;52:134–7.
  66. De Langen AJ, Klabbers B, Lubberink M, Boellaard R, Spreeuwenberg MD, Slotman BJ, et al. Reproducibility of quantitative (18)F-3'-Deoxy-3'-fluorothymidine measurements using positron emission tomography. *Eur J Nucl Med Mol Imaging.* 2009;36:389–95. <https://doi.org/10.1007/S00259-008-0960-5>.
  67. Vesselle H, Grierson J, Muzi M, Pugsley JM, Schmidt RA, Rabinowitz P, et al. In vivo validation Of 3' Deoxy-3' [F-18]fluorothymidine ([F-18]FLT) as a proliferation imaging tracer in humans: correlation of [F-18]FLT uptake by positron emission tomography with Ki-67 immunohistochemistry and flow cytometry in human lung tumors. *Clin Cancer Res.* 2002;8:3315–23.
  68. Pan MH, Huang SC, Liao YP, Schae D, Wang CC, Stout DB, et al. FDG-PET imaging of radiation responses in murine tumors. *Mol Imaging Biol.* 2008;10:325–34. <https://doi.org/10.1007/S11307-008-0158-Z>.
  69. Contractor KB, Kenny LM, Stebbing J, Challapalli A, Al-Nahhas A, Palmieri C, et al. Biological basis of [(11)C]choline-positron emission tomography in patients with breast cancer: comparison with [(18)F]fluorothymidine positron emission tomography. *Nucl Med Comm.* 2011;32:997–1004. <https://doi.org/10.1097/Mnm.0b013e328349567b>.
  70. Backes H, Ullrich R, Neumaier B, Kracht L, Wienhard K, Jacobs AH. Noninvasive quantification of (18)F-FLT human brain PET for the assessment of tumour proliferation in patients with high-grade glioma. *Eur J Nucl Med Mol Imaging.* 2009;36:1960–7. <https://doi.org/10.1007/S00259-009-1244-4>.
  71. Brenner W, Vernon C, Muzi M, Mankoff DA, Link JM, Conrad EU, et al. Comparison of different quantitative approaches to 18F-fluoride PET scans. *J Nucl Med.* 2004;45:1493–500.
  72. Siddique M, Frost ML, Blake GM, Moore AE, Al-Beyatti Y, Marsden PK, et al. The precision and sensitivity of 18F-fluoride PET for measuring regional bone metabolism: a comparison of quantification methods. *J Nucl Med.* 2011;52:1748–55.
  73. Lubberink M, Sandstrom M, Sörensen J, Granberg D, Garske-Román U, Lundqvist H, et al. Tracer kinetic analysis of 68ga-DOTATATE and 68ga-DOTATOC in neuroendocrine tumours. *J Nucl Med.* 2013;54:200.
  74. Velikyan I, Sundin A, Sörensen J, Lubberink M, Sandström M, Garske-Román U, et al. Quantitative and qualitative intrapatient comparison of 68ga-DOTATOC and 68ga-68ga-DOTATATE: net uptake rate for accurate quantification. *J Nucl Med.* 2014;55:204–10.
  75. Menda Y, Ponto LLB, Schultz MK, Zamba GK, Watkins GL, Bushnell DL, et al. Repeatability of 68ga-DOTATOC PET imaging in neuroendocrine tumors. *Pancreas.* 2013;42:937.
  76. Bentourkia M, Zaidi H. Tracer kinetic modeling in PET. *Pet Clinics.* 2007;2:267–77.
  77. Carson RE. Tracer kinetic modeling in PET. In: Valk PE, Bailey DL, Townsend DW, Maisey MN (eds) *Positron emission tomography: basic science and clinical practice.* London: Springer; 2005. pp 127–59.
  78. Zhu W, Li Q, Bai B, Conti PS, Leahy RM. Patlak image estimation from dual time-point list-mode pet data. *IEEE T Med Imaging.* 2014;33:913–24.
  79. Gjedde A. Positron emission tomography of brain glucose metabolism with [18F] fluorodeoxyglucose in humans. In: Hirrlinger J, Waagepetersen HS (eds) *Brain energy metabolism.* London: Springer; 2014. pp 341–64.
  80. Karakatsanis N, Lodge M, Zhou Y, Casey M, Wahl R, Subramaniam R, et al. Novel multi-parametric SUV/Patlak FDG-PET whole-body imaging framework for routine application to clinical oncology. *J Nucl Med.* 2015;56:625.
  81. Zhou Y, Lodge M, Crandall J, Karakatsanis N, Casey M, Ashrafinia S, et al. Evaluation of whole-body parametric PET/CT image generation from high resolution high sensitivity mCT scanner. *J Nucl Med.* 2015;56:372.
  82. Karakatsanis NA, Casey ME, Knesaurek K, Fayad ZA, Kostakoglu L. SUV/Patlak-4D whole-body PET/CT dynamic and parametric imaging: clinical demonstration and validation of SUV synthesis from dynamic passes. *IEEE NSS/MIC.* Atlanta, Ga: IEEE; 2017.
  83. Osborne DR, Acuff S. Whole-body dynamic imaging with continuous bed motion PET/CT. *Nucl Med Commun.* 2016;37:428.
  84. Dweck MR, Abgral R, Trivieri MG, Robson PM, Karakatsanis N, Mani V, et al. Hybrid magnetic resonance imaging and positron emission tomography with fluorodeoxyglucose to diagnose active cardiac sarcoidosis. *JACC Cardiovasc Imaging.* 2018;11:94–107.
  85. Den Hoff J, Hofheinz F, Oehme L, Schramm G, Langner J, Beuthien-Baumann B, et al. Dual time point based quantification of metabolic uptake rates in 18F-FDG PET. *EJNMMI Res.* 2013;3:16. <https://doi.org/10.1186/2191-219x-3-16>.
  86. Hustinx R, Smith RJ, Benard F, Rosenthal DI, Machtay M, Farber LA, et al. Dual time point fluorine-18 fluorodeoxyglucose positron emission tomography: a potential method to differentiate malignancy from inflammation and normal tissue in the head and neck. *Eur J Nucl Med Mol Imaging.* 1999;26:1345–8.
  87. Sanz-Viedma S, Torigian DA, Parsons M, Basu S, Alavi A. Potential clinical utility of dual time point FDG-PET for distinguishing benign from malignant lesions: implications for oncological imaging. *Rev Esp Med Nucl Imagen Mol.* 2009;28:159–66.
  88. Gambhir SS, Schwaiger M, Huang S-C, Krivokapich J, Schelbert HR, Nienaber CA, et al. Simple noninvasive quantification method for measuring myocardial glucose utilization in humans employing positron emission tomography and fluorine-18 deoxyglucose. *J Nucl Med.* 1989;30:359–66.
  89. Chen K, Bandy D, Reiman E, Huang SC, Lawson M, Feng D, et al. Noninvasive quantification of the cerebral metabolic rate for glucose using positron emission tomography, 18F-fluoro-2-deoxyglucose, the Patlak method, and an image-derived input function. *J Cereb Blood Flow Metab.* 1998;18:716–23.
  90. Wu HM, Hoh CK, Choi Y, Schelbert HR, Hawkins RA, Phelps ME, et al. Factor analysis for extraction of blood time-activity curves in dynamic FDG-PET studies. *J Nucl Med.* 1995;36:1714–22.
  91. Bengel FM, Higuchi T, Javadi MS, Lautamaki R. Cardiac positron emission tomography. *J Am Coll Cardiol.* 2009;54:1–15.



92. Lodge M, Bengel F. Methodology for quantifying absolute myocardial perfusion with PET and SPECT. *Curr Cardiol Rep.* 2007;9: 121–8.
93. Hove JD, Iida H, Kofoed KF, Freiberg J, Holm S, Kelbaek H. Left atrial versus left ventricular input function for quantification of the myocardial blood flow with nitrogen-13 ammonia and positron emission tomography. *Eur J Nucl Med Mol Imaging.* 2004;31:71–6.
94. Zanotti-Fregonara P, Fadaili EM, Maroy R, Comtat C, Souloumiac A, Jan S, et al. Comparison of eight methods for the estimation of the image-derived input function in dynamic [18F]-FDG PET human brain studies. *J Cereb Blood Flow Metab.* 2009;29:1825–35.
95. De Geus-Oei L-F, Visser EP, Krabbe PF, Van Hoorn BA, Koenders EB, Willemsen AT, et al. Comparison of image-derived and arterial input functions for estimating the rate of glucose metabolism in therapy-monitoring [18F]-FDG PET studies. *J Nucl Med.* 2006;47:945–9.
96. Feng D, Huang S-C, Wang X. Models for computer simulation studies of input functions for tracer kinetic modeling with positron emission tomography. *Int J Biomed Comput.* 1993;32:95–110.
97. Takikawa S, Dhawan V, Spetsieris P, Robeson W, Chaly T, Dahl R, et al. Noninvasive quantitative fluorodeoxyglucose PET studies with an estimated input function derived from a population-based arterial blood curve. *Radiology.* 1993;188:131–6.
98. Eberl S, Anayat AR, Fulton RR, Hooper PK, Fulham MJ. Evaluation of two population-based input functions for quantitative neurological FDG PET studies. *Eur J Nucl Med.* 1997;24: 299–304.
99. Vriens D, De Geus-Oei L-F, Oyen WJ, Visser EP. A curve-fitting approach to estimate the arterial plasma input function for the assessment of glucose metabolic rate and response to treatment. *J Nucl Med.* 2009;50:1933–9.
100. Karakatsanis N, Zhou Y, Lodge M, Casey M, Wahl R, Subramaniam R, et al. Clinical whole-body PET Patlak imaging 60–90min post-injection employing a population-based input function. *J Nucl Med.* 2015;56:1786.
101. Lodge MA. Repeatability of SUV in oncologic 18F-FDG PET. *J Nucl Med.* 2017;58:523–32.
102. Karakatsanis NA, Lodge MA, Casey ME, Zaidi H, Rahmim A. Impact of acquisition time-window on clinical whole-body PET parametric imaging. *Nuclear Science Symposium and Medical Imaging Conference (NSS/MIC), 2014 IEEE: IEEE;* 2014. pp 1–8.
103. Kaneta T, Takai Y, Iwata R, Hakamatsuka T, Yasuda H, Nakayama K, et al. Initial evaluation of dynamic human imaging using 18 F-FRP170 as a new PET tracer for imaging hypoxia. *Ann Nucl Med.* 2007;21:101–7.
104. Karakatsanis NA, Casey ME, Lodge MA, Rahmim A, Zaidi H. Whole-body direct 4D parametric PET imaging employing nested generalized Patlak expectation–maximization reconstruction. *Phys Med Biol.* 2016;61:5456.
105. Karakatsanis NA, Zhou Y, Lodge MA, Casey ME, Wahl RL, Zaidi H, et al. Generalized whole-body Patlak parametric imaging for enhanced quantification in clinical PET. *Phys Med Biol.* 2015;60: 8643.
106. Wang Q, Wang R-F, Zhang J, Zhou Y. Differential diagnosis of pulmonary lesions by parametric imaging in 18F-FDG PET/CT dynamic multi-bed scanning. *J Buon.* 2013;18:928–34.
107. Panin V, Bal H, Defrise M, Casey M, Karakatsanis N, Rahmim A. Whole body parametric imaging on clinical scanner: direct 4D reconstruction with simultaneous attenuation estimation and time-dependent normalization. *Nuclear Science Symposium And Medical Imaging Conference (NSS/MIC), 2015 IEEE: IEEE;* 2015. 7pp.
108. Karakatsanis NA, Garibotto V, Rager O, Zaidi H. Continuous bed motion vs. step-and-shoot acquisition on clinical whole-body dynamic and parametric PET imaging. *Nuclear Science Symposium And Medical Imaging Conference (NSS/MIC), 2015 IEEE: IEEE;* 2015. 6pp.
109. Kotasidis FA, Garibotto V, Zaidi H. Hybrid whole-body dynamic TOF PET imaging for simultaneous estimation of compartmental and Patlak parametric maps from continuous bed motion data. *Nuclear Science Symposium, Medical Imaging Conference and Room-Temperature Semiconductor Detector Workshop (NSS/MIC/RTSD): IEEE;* 2016. 2pp.
110. Kotasidis FA, Manari M, Garibotto V, Zaidi H. Joint optimization of kinetic modelling and CBM acquisition parameters in hybrid whole-body dynamic PET imaging. *Nuclear Science Symposium, Medical Imaging Conference and Room-Temperature Semiconductor Detector Workshop (NSS/MIC/RTSD): IEEE;* 2017. 2pp.
111. Jang H, Im HJ, Rahmim A, Cho S, Mcmillan A. On the feasibility of quantitative dynamic whole body PET/MR imaging. *Proc Intl Soc Mag Reson Med.* 2016;24:3715.
112. Lodge M, Rahmim A, Antoniou A, Solnes L, Wahl R. Dynamic whole-body 68ga-DOTATOC PET/CT. *J Nucl Med.* 2015;56(Suppl. 3):648.
113. Johansson E, Lubberink M, Heurling K, Eriksson JW, Skrtic S, Ahlström H, et al. Whole-body imaging of tissue-specific insulin sensitivity and body composition by using an integrated PET/MR system: a feasibility study. *Radiology.* 2017;286:271–8.
114. Naganawa M, Gallezot JD, Shah V, Smith AM, Carson RE. The influence of sampling schedule for image-derived input function and Patlak plot estimation in whole body PET studies. *IEEE Nucl Sci Symp Conf Theatr Rec* 2017.
115. Zhou Y, Huang SC, Bergsneider M, Wong DF. Improved parametric image generation using spatial–temporal analysis of dynamic PET studies. *NeuroImage.* 2002;15:697–707. <https://doi.org/10.1006/Nimg.2001.1021>.
116. Zhou Y, Endres CJ, Brasic JR, Huang SC, Wong DF. Linear regression with spatial constraint to generate parametric images of ligand-receptor dynamic PET studies with a simplified reference tissue model. *NeuroImage.* 2003;18:975–89. [https://doi.org/10.1016/S1053-8119\(03\)00017-X](https://doi.org/10.1016/S1053-8119(03)00017-X).
117. Huang X, Zhou Y, Bao S, Huang SC. Clustering-based linear least square fitting method for generation of parametric images in dynamic FDG PET studies. *Int J Biomed Imaging.* 2007;2007: 65641.
118. Mohy-Ud-Din H, Lodge MA, Rahmim A. Quantitative myocardial perfusion PET parametric imaging at the voxel-level. *Phys Med Biol.* 2015;60:6013.
119. Bal H, Panin V, Karakatsanis N, Lodge M, Rahmim A, Casey M. Novel quantitative whole-body parametric pet imaging utilizing multiple clustering realizations. *Nuclear Science Symposium, Medical Imaging Conference and Room-Temperature Semiconductor Detector Workshop (NSS/MIC/RTSD), 2016: IEEE;* 2016. 5pp.
120. Van Slambrouck K, Stute S, Comtat C, Sibomana M, Van Velden F, Boellaard R. Et Al. Bias reduction for low-statistics PET: maximum likelihood reconstruction with a modified Poisson distribution. *IEEE T Med Imaging.* 2015;34:126–36.
121. Barrett HH, Wilson DW, Tsui BMW. Noise properties of the EM algorithm. *I Theory Phys Med Biol.* 1994;39:833–46.
122. Qi J. A unified noise analysis for iterative image estimation. *Phys Med Biol.* 2003;48:3505–19.
123. Tsoumpas C, Turkheimer FE, Thielemans K. A survey of approaches for direct parametric image reconstruction in emission tomography. *Med Phys.* 2008;35:3963–71.
124. Rahmim A, Tang J, Zaidi H. Four-dimensional (4D) image reconstruction strategies in dynamic PET: beyond conventional independent frame reconstruction. *Med Phys.* 2009;36:3654–70.



125. Wang G, Qi J. Direct estimation of kinetic parametric images for dynamic PET. *Theranostics* 2013; 3(10):802–815.
126. Huang SC, Carson RE, Phelps ME. Measurement of local blood flow and distribution volume with short-lived isotopes: a general input technique. *J Cereb Blood Flow Metab.* 1982;2:99–108.
127. Alpert NM, Eriksson L, Chang JY, Bergstrom M, Litton JE, Correia JA, et al. Strategy for the measurement of regional cerebral blood flow using short-lived tracers and emission tomography. *J Cereb Blood Flow Metab.* 1984;4:28–34.
128. Maguire RP, Calonder C, Leenders KL. An investigation of multiple time/graphical analysis applied to projection data: theory and validation. *J Comput Assist Tomogr.* 1997;21:327–31.
129. Carson RE, Lange K. The EM parametric image reconstruction algorithm. *J Am Statist Assoc.* 1985;80:20–2.
130. Matthews J, Bailey D, Price P, Cunningham V. The direct calculation of parametric images from dynamic PET data using maximum-likelihood iterative reconstruction. *Phys Med Biol.* 1997;42:1155.
131. Kamasak ME, Bouman CA, Morris ED, Sauer K. Direct reconstruction of kinetic parameter images from dynamic PET data. *IEEE Trans Med Imaging.* 2005;24:636–50.
132. Wang G, Fu L, Qi J. Maximum a posteriori reconstruction of the Patlak parametric image from sinograms in dynamic PET. *Phys Med Biol.* 2008;53:593–604.
133. Tsoumpas C, Turkheimer FE, Thielemans K. Study of direct and indirect parametric estimation methods of linear models in dynamic positron emission tomography. *Med Phys.* 2008;35:1299–309.
134. Tang J, Kuwabara H, Wong DF, Rahmim A. Direct 4D reconstruction of parametric images incorporating anato-functional joint entropy. *Phys Med Bio.* 2010;55:1–12.
135. Wang G, Qi J. Acceleration of the direct reconstruction of linear parametric images using nested algorithms. *Phys Med Biol.* 2010;55:1505–17.
136. Barrett HH, Myers KJ. *Foundations of image science.* Hoboken, New Jersey: Wiley & Sons, Inc.; 2004.
137. Anzai Y, Minoshima S, Wolf GT, Wahl RL. Head and neck cancer: detection of recurrence with three-dimensional principal components analysis at dynamic FDG PET. *Radiology.* 1999;212:285–90.
138. Pedersen F, Bergströme M, Bengtsson E, Långström B. Principal component analysis of dynamic positron emission tomography images. *Eur J Nucl Med.* 1994;21:1285–92.
139. Thireou T, Strauss LG, Dimitrakopoulou-Strauss A, Kontaxakis G, Pavlopoulos S, Santos A. Performance evaluation of principal component analysis in dynamic FDG-PET studies of recurrent colorectal cancer. *Comput Med Imaging Graph.* 2003;27:43–51.
140. Razifar P, Axelsson J, Schneider H, Långström B, Bengtsson E, Bergström MA. New application of pre-normalized principal component analysis for improvement of image quality and clinical diagnosis in human brain PET studies—clinical brain studies using [11c]-Gr205171,[11c]-L-deuterium-deprenyl,[11c]-5-hydroxy-L-tryptophan,[11c]-L-dopa and Pittsburgh compound-B. *NeuroImage.* 2006;33:588–98.
141. Lee JS, Lee DS, Ahn JY, Cheon GJ, Kim S-K, Yeo JS, et al. Blind separation of cardiac components and extraction of input function from H215O dynamic myocardial PET using independent component analysis. *J Nucl Med.* 2001;42:938–43.
142. Naganawa M, Kimura Y, Ishii K, Oda K, Ishiwata K, Matani A. Extraction of a plasma time-activity curve from dynamic brain PET images based on independent component analysis. *IEEE Trans Biomed Eng.* 2005;52:201–10.
143. Ahn JY, Lee DS, Lee JS, Kim S-K, Cheon GJ, Yeo JS, et al. Quantification of regional myocardial blood flow using dynamic H215O PET and factor analysis. *J Nucl Med.* 2001;42:782–7.
144. El Fakhri G, Sitek A, Guérin B, Kijewski MF, Di Carli MF, Moore SC. Quantitative dynamic cardiac 82Rb PET using generalized factor and compartment analyses. *J Nucl Med.* 2005;46:1264–71.
145. Su Y, Welch MJ, Shoghi KI. The application of maximum likelihood factor analysis (MLFA) with uniqueness constraints on dynamic cardiac microPET data. *Phys Med Biol.* 2007;52:2313.
146. El Fakhri G, Trott CM, Sitek A, Bonab A, Alpert NM. Dual-tracer PET using generalized factor analysis of dynamic sequences. *Mol Imaging Biol.* 2013;15:666–74.
147. Veronese M, Rizzo G, Bertoldo A, Turkheimer FE. Spectral analysis of dynamic PET studies: a review of 20 years of method developments and applications. *Comput Math Methods Med.* 2016;2016:7187541.
148. Cunningham VJ, Ashburner J, Byrne H, Jones T (1993) Use of spectral analysis to obtain parametric images from dynamic PET studies. In: Uemura K, Lassen NA, Jones T, Kanno I (eds) *Quantification of brain function. Tracer kinetics and image analysis in brain PET.* Amsterdam, Elsevier Science, pp 101–108
149. Wong K-P, Feng D, Meikle SR, Fulham MJ. Segmentation of dynamic PET images using cluster analysis. *IEEE Trans Nucl Sci.* 2002;49:200–7.
150. Dimitrakopoulou-Strauss A, Pan L, Strauss LG. Parametric imaging: a promising approach for the evaluation of dynamic PET-18F-FDG studies — the DKFZ experience. *Hell J Nucl Med.* 2010;13: 18–22.
151. Slobbe P, Poot AJ, Windhorst AD, Van Dongen GA. PET imaging with small-molecule tyrosine kinase inhibitors: TKI-PET. *Drug Discov Today.* 2012;17:1175–87.
152. Foster JA, Neufeld KAM. Gut-brain axis: how the microbiome influences anxiety and depression. *Trends Neurosci* 2013;36:305–312.
153. Chandra R, Hiniker A, Kuo Y-M, Nussbaum RI, Liddle RA. A-Synuclein in gut endocrine cells and its implications for Parkinson's disease. *JCI Insight* 2017;2(12):pii: 92295.
154. Mulak A, Bonaz B. Brain-gut-microbiota axis in Parkinson's disease. *World J Gastroenterol.* 2015;21:10609–20.
155. Tahsili-Fahadan P, Geocadin RG. Heart-brain axis: effects of neurologic injury on cardiovascular function. *Circ Res.* 2017;120: 559–72.
156. Thackeray JT, Hupe HC, Wang Y, Bankstahl JP, Berding G, Ross TL, et al. Myocardial inflammation predicts remodeling and neuroinflammation after myocardial infarction. *J Am Coll Cardiol.* 2018;71:263–75.
157. Tawakol A, Ishai A, Takx RA, Figueroa AL, Ali A, Kaiser Y, et al. Relation between resting amygdalar activity and cardiovascular events: a longitudinal and cohort study. *Lancet.* 2017;389:834–845.
158. Seemann MD. Whole-body PET/MRI: the future in oncological imaging. *Technol Cancer Res Treat.* 2005;4:577–82.
159. Pichler BJ, Kolb A, Nägele T, Schlemmer H-P. PET/MRI: paving the way for the next generation of clinical multimodality imaging applications. *J Nucl Med.* 2010;51:333–6.
160. Yankeelov TE, Peterson TE, Abramson RG, Garcia-Izquierdo D, Arlinghaus LR, Li X, et al. Simultaneous PET-MRI in oncology: a solution looking for a problem? *Magn Reson Imaging.* 2012;30: 1342–56.
161. Zaidi H, Becker M. The promise of hybrid PET/MRI: technical advances and clinical applications. *IEEE Signal Process Mag.* 2016;33:67–85.
162. Moser E, Stadlbauer A, Windischberger C, Quick HH, Ladd ME. Magnetic resonance imaging methodology. *Eur J Nucl Med Mol Imaging.* 2009;36:30–41. <https://doi.org/10.1007/S00259-008-0938-3>.
163. Halpern BS, Dahlbom M, Quon A, Schiepers C, Waldherr C, Silverman DH, et al. Impact of patient weight and emission scan duration on PET/CT image quality and lesion detectability. *J Nucl Med.* 2004;45:797–801.

164. Kotasidis FA, Tsoumpas C, Rahmim A. Advanced kinetic modeling strategies: towards adoption in clinical PET imaging. *Clin Trans Imag*. 2014;2:219–37.
165. Catana C. Motion correction options in PET/MRI. *Semin Nucl Med*. 2015; 45(3):212–23.
166. Sadeghi MM, Glover DK, Lanza GM, Fayad ZA, Johnson LL. Imaging atherosclerosis and vulnerable plaque. *J Nucl Med*. 2010;51:51s–65s.
167. Rudd JH, Narula J, Strauss HW, Virmani R, Machac J, Klimas M, et al. Imaging atherosclerotic plaque inflammation by fluorodeoxyglucose with positron emission tomography: ready for prime time? *J Am Coll Cardiol*. 2010;55:2527–2535.
168. Fayad ZA, Fuster V, Fallon JT, Jayasundera T, Worthley SG, Helft G, et al. Noninvasive in vivo human coronary artery lumen and wall imaging using black-blood magnetic resonance imaging. *Circulation*. 2000;102:506–10.
169. Sanz J, Fayad ZA. Imaging of atherosclerotic cardiovascular disease. *Nature*. 2008;451:953–7.
170. Oo J, Karakatsanis N, Rahmim A, Lodge M, Wahl R. A novel imaging method for assessing vessel wall inflammation: dynamic multi-bed PET parametric imaging. *J Nucl Med*. 2013;54:1670.
171. Ravina B, Eidelberg D, Ahlskog JE, Albin RL, Brooks DJ, Carbon M, et al. The role of radiotracer imaging in Parkinson disease. *Neurology*. 2005;64:208–15. <https://doi.org/10.1212/01.Wnl.0000149403.14458.7f>.
172. Cherry SR, Jones T, Karp JS, Qi J, Moses WW, Badawi RD. Total-body PET: maximizing sensitivity to create new opportunities for clinical research and patient care. *J Nucl Med*. 2018;59:3–12.
173. Verhaeghe J, Gravel P, Mio R, Fukasawa R, Rosa-Neto P, Soucy JP, et al. Motion compensation for fully 4D pet reconstruction using PET superset data. *Phys Med Biol*. 2010;55:4063–82. <https://doi.org/10.1088/0031-9155/55/14/008>
174. Nakamoto Y, Sakamoto S, Okada T, Matsumoto K, Minota E, Kawashima H, et al. Accuracy of image fusion using a fixation device for whole-body cancer imaging. *AJR Am J Roentgenol*. 2005;184:1960–6.
175. Munk OL, Bass L, Roelsgaard K, Bender D, Hansen SB, Keiding S. Liver kinetics of glucose analogs measured in pigs by PET: importance of dual-input blood sampling. *J Nucl Med*. 2001;42: 795–801.
176. Scussolini M, Garbarino S, Sambuceti G, Caviglia G, Piana M. A Physiology-based parametric imaging method for FDG-PET data. *Inverse Problems*. 2017;33:125010.